

# Formation of double glass in binary mixtures of anisotropic particles: Dynamic heterogeneities in rotations and displacements

Kyohei Takae and Akira Onuki

*Department of Physics, Kyoto University, Kyoto 606-8502, Japan*

(Dated: September 15, 2021)

We study glass behavior in a mixture of elliptic and circular particles in two dimensions at low temperatures using an orientation-dependent Lennard-Jones potential. The ellipses have a mild aspect ratio ( $\sim 1.2$ ) and tend to align at low temperatures, while the circular particles play the role of impurities disturbing the ellipse orientations at a concentration of 20%. These impurities have a size smaller than that of the ellipses and attract them in the homeotropic alignment. As a result, the coordination number around each impurity is mostly five or four in glassy states. We realize double glass, where both the orientations and the positions are disordered but still hold mesoscopic order. We find a strong heterogeneity in the flip motions of the ellipses, which sensitively depends on the impurity clustering. In our model, a small fraction of the ellipses still undergo flip motions relatively rapidly even at low temperatures. In contrast, the non-flip rotations (with angle changes not close to  $\pm\pi$ ) are mainly caused by the cooperative configuration changes involving many particles. Then, there arises a long-time heterogeneity in the non-flip rotations closely correlated with the dynamic heterogeneity in displacements.

PACS numbers: 64.70.Q-, 64.70.P-, 61.20.Lc, 61.43.Fs

## I. INTRODUCTION

Much attention has been paid to various types of glass transitions, where the structural relaxations become extremely slow with lowering the temperature  $T$  [1, 2]. In experiments, colloidal particles can be spherical, but real molecules are mostly nonspherical. The translational and rotational diffusion constants have thus been measured in molecular systems near the glass transition [3]. Using generalized mode-coupling theories, some authors [4–6] have studied the coupled translation-rotation dynamics to predict translational glass and orientational glass. Theoretically, for double glass [6], the translational and orientational degrees of freedom can be simultaneously arrested at the same temperature. In real systems, the molecular rotations sensitively depend on many parameters including the molecular shapes, the density and the concentration (for mixtures).

Mixtures of anisotropic particles with mild differences in sizes and shapes such as  $(\text{KCN})_x(\text{KBr})_{1-x}$  form a cubic crystal without orientational order (plastic solid) at relatively high  $T$ . With further lowering  $T$ , they undergo a structural phase transition in dilute cases and become orientational glass in nondilute cases [7], where the crystal structure is preserved. On the other hand, if the two species have significantly different sizes or shapes, translational glass without crystal order can emerge from liquid at low  $T$ . For rodlike molecules with relatively large aspect ratios, liquid crystal phase transitions occur with lowering  $T$ , but their glass transitions have not yet well understood. In recent experiments on colloidal ellipsoids in monolayers, the aspect ratio was 6 [8] or 2.1 [9] with considerable size dispersities. In glassy states, these ellipsoids exhibited mesoscopic nematic or smectic order.

Molecular dynamics simulations have also been performed on glass-forming fluids composed of anisotropic

particles. They can be one-component fluids with a complex internal structure. Examples are methanol [10], ortho-terphenyl methanol (OTP) [11, 12], and fluids of asymmetric dumbbells [13, 14]. There are various kinds of two-component glass-formers. The simplest example is a mixture of two species of symmetric dumbbells [15–17]. Recently, we studied a mixture of spheroidal and spherical particles to examine the orientational glass using an orientation-dependent potential [18].

The physical picture of double glass is thus very complex. To give a clear example, we consider a mixture of elliptic particles with a mild aspect ratio and smaller circular particles (impurities). We assume orientation-dependent repulsive and attractive interactions, where the attractive part is between the ellipses and the impurities. Then, the impurities can strongly disturb the orientations and the positions of the surrounding ellipses. This is analogous to hydration of ions by surrounding water molecules [19, 20]. If the impurity concentration  $c$  is increased from zero, orientational domains and crystalline grains of the ellipses are gradually fragmented and disordered [18]. In this paper, we realize double glass at low  $T$  at an impurity concentration of 20%.

To produce glassy states, we slowly quench the mixture from liquid. In this situation, we encounter impurity clustering or aggregation at low  $T$ , which often results in small crystalline domains of impurities [21, 22]. In our model, this tendency is considerably suppressed by the above-mentioned impurity-ellipse attractive interaction. Nevertheless, the impurity distribution is still mesoscopically heterogeneous, leading to a mesoscopic heterogeneity in the rotational motions. We shall see that some fraction of the ellipses still rotate under weak constraints even at low  $T$ . Furthermore, if anisotropic particles have the elliptic symmetry (the spheroidal one in three dimensions), they can undergo flip (turnover) motions with  $\pm\pi$

angle changes [10, 13, 14]. These flip motions can occur thermally for mild aspect ratios, while they are sterically hindered by the surrounding particles for large aspect ratios. Thus, we expect a wide range of the rotational activity for mild aspect ratios.

We shall find marked orientational and positional heterogeneities on mesoscopic scales in glass. Such heterogeneous patterns have been visualized in various model systems [23–25]. First, there arises a mesoscopic heterogeneity of the flip motions correlated with the impurity clustering. Second, the positional configuration changes cause non-flip rotations of the ellipses, which are the origin of the long-time decay of the rotational correlation functions  $G_\ell(t)$  of even  $\ell$  [10, 12–17]. It follows a dynamic heterogeneity of the long-time non-flip rotations correlated with the dynamic heterogeneity in displacements or bond breakage [26–29].

The organization of this paper is as follows. In Sec.II, we will explain our simulation model and method. In Sec.IIIA, we will present simulation results on the heterogeneities in the orientations and the positions. In Sec.IIIB, the time-correlation functions will be examined. In Sec.IIIC, the angular and translational mean-square displacements will be calculated. In Sec.IIID, we will introduce the flip number for each ellipse in a time interval and study its heterogeneity. In Sec.IIIE, time-development of a configurational change with large displacements and/or large angle changes will be illustrated.

## II. MODEL AND NUMERICAL METHOD

In two dimensions, we consider mixtures of anisotropic and circular particles with numbers  $N_1$  and  $N_2$ , where  $N = N_1 + N_2 = 4096$ . The concentration of the circular species is  $c = N_2/N$ . The particle positions are written as  $\mathbf{r}_i$  ( $i = 1, \dots, N$ ). The orientation vectors of the anisotropic particles are expressed as  $\mathbf{n}_i = (\cos \theta_i, \sin \theta_i)$  in terms of angles  $\theta_i$  ( $i = 1, \dots, N_1$ ). The pair potential  $U_{ij}$  between particles  $i \in \alpha$  and  $j \in \beta$  ( $\alpha, \beta = 1, 2$ ) is a modified Lennard-Jones potential given by [18]

$$U_{ij} = 4\epsilon \left[ (1 + A_{ij}) \frac{\sigma_{\alpha\beta}^{12}}{r_{ij}^{12}} - (1 + B_{ij}) \frac{\sigma_{\alpha\beta}^6}{r_{ij}^6} \right], \quad (1)$$

where  $r_{ij}$  is the particle distance and  $\epsilon$  is the interaction energy. In terms of characteristic lengths  $\sigma_1$  and  $\sigma_2$ , we set  $\sigma_{\alpha\beta} = (\sigma_\alpha + \sigma_\beta)/2$ . The potential is truncated at  $r_{ij} = 3\sigma_1$ . The particle anisotropy is accounted for by the anisotropic factors  $A_{ij}$  and  $B_{ij}$ , which depend on the angles between  $\mathbf{n}_i$ ,  $\mathbf{n}_j$ , and the relative direction  $\hat{\mathbf{r}}_{ij} = r_{ij}^{-1}(\mathbf{r}_i - \mathbf{r}_j)$ . In this paper, we set

$$A_{ij} = \chi[\delta_{\alpha 1}(\mathbf{n}_i \cdot \hat{\mathbf{r}}_{ij})^2 + \delta_{\beta 1}(\mathbf{n}_j \cdot \hat{\mathbf{r}}_{ij})^2], \quad (2)$$

$$B_{ij} = \zeta[\delta_{\alpha 1}\delta_{\beta 2}(\mathbf{n}_i \cdot \hat{\mathbf{r}}_{ij})^2 + \delta_{\alpha 2}\delta_{\beta 1}(\mathbf{n}_j \cdot \hat{\mathbf{r}}_{ij})^2], \quad (3)$$

where  $\delta_{\alpha\beta}$  is the Kronecker delta,  $\chi$  is the anisotropy strength of repulsion, and  $\zeta$  is that of attraction between the two species.

The Newton equations for  $\mathbf{r}_i(t)$  and  $\theta_i(t)$  are given by

$$m \frac{d^2}{dt^2} \mathbf{r}_i = - \frac{\partial U}{\partial \mathbf{r}_i}, \quad (4)$$

$$I \frac{d^2}{dt^2} \theta_i = - \frac{\partial U}{\partial \theta_i}, \quad (5)$$

where  $U = \sum_{i < j} U_{ij}$  is the total potential,  $m$  is the mass common to the two species, and  $I$  is the moment of inertia. Note that Eq.(5) holds for the first species. The total kinetic energy is given by  $K = \sum_i m |d\mathbf{r}_i/dt|^2/2 + \sum_{i \leq N_1} I |d\theta_i/dt|^2/2$ . Here,  $d\theta_i/dt$  is continuous in time and  $\theta_i$  is unbounded.

We regard the anisotropic particles as ellipses. For two anisotropic particles  $i$  and  $j$ ,  $U_{ij}$  is minimized at  $r_{ij} = 2^{1/6}(1 + A_{ij})^{1/6}\sigma_1$  as a function of  $r_{ij}$  for fixed orientations. Then  $A_{ij}$  is minimum for  $\mathbf{n}_i$  and  $\mathbf{n}_j$  being perpendicular to  $\hat{\mathbf{r}}_{ij}$ , while it is maximum for  $\mathbf{n}_i$  and  $\mathbf{n}_j$  being parallel to  $\pm \hat{\mathbf{r}}_{ij}$ . The shortest and longest diameters are given by

$$a_s = 2^{1/6}\sigma_1, \quad a_\ell = (1 + 2\chi)^{1/6}2^{1/6}\sigma_1. \quad (6)$$

The aspect ratio is thus

$$a_\ell/a_s = (1 + 2\chi)^{1/6}. \quad (7)$$

These ellipses have the area  $S_1 = \pi a_s a_\ell/4$  and the momentum of inertia  $I = (a_\ell^2 + a_s^2)m_1/16$ .

In this paper, we fixed the average packing fraction  $(S_1 N_1 + S_2 N_2)/L^2$  at 0.95, where  $S_2 = \pi 2^{1/3}\sigma_2^2/4$ . The cell length  $L$  is about  $70\sigma_1$ . We measure space in units of  $\sigma_1$  and time in units of

$$\tau_0 = \sigma_1 \sqrt{m/\epsilon}. \quad (8)$$

The temperature is in units of  $\epsilon/k_B$ , where  $k_B$  is the Boltzmann constant. In this paper, assuming small circular impurities, we set

$$\sigma_2/\sigma_1 = 0.6, \quad \chi = 1.2, \quad c = 0.2. \quad (9)$$

The aspect ratio is then  $a_\ell/a_s = 1.23$  from Eq.(7), which is rather close to unity. If the aspect ratio is considerably larger than unity, liquid crystal order appears at higher temperatures than in this paper.

We integrated the Newton equations using the leap-frog method under the periodic boundary condition. We lowered  $T$  from 1 to 0.1 at a cooling rate of  $dT/dt = 0.9 \times 10^{-5}$ . We then changed  $T$  to a final temperature and waited for  $2 \times 10^5$ , where a Nosé-Hoover thermostat [33] was imposed. But after this initial preparation, we switched off the thermostat, so our simulations have been performed in the  $NVE$  ensemble, where the average translational kinetic energy was kept at  $k_B T$  per particle.

Previously, angle-dependent potentials were used for liquid crystals [22, 30], water [31], glass-forming liquids [24], and lipids [32]. Our mixture system is similar to that of prolate Gay-Berne particles [30] and Lennard-Jones spheres studied by Antypov and Cleaver [22].

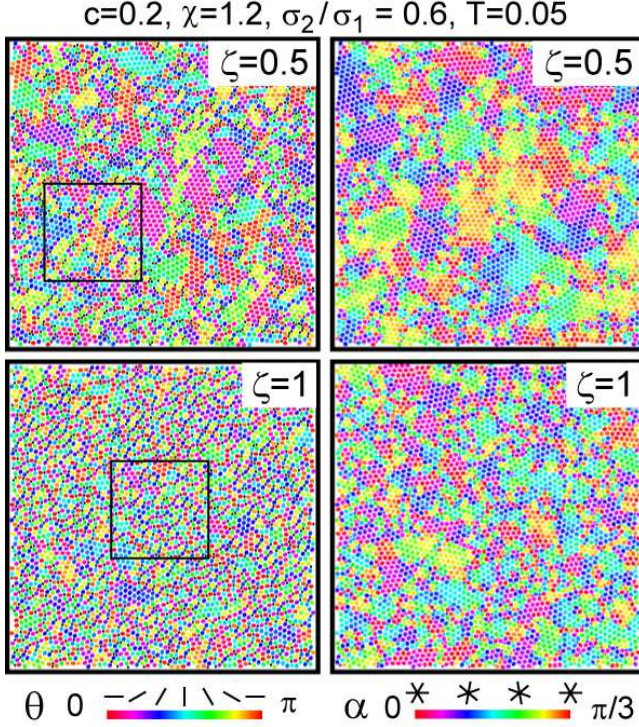


FIG. 1. (Color online) Orientational angles  $\theta_j$  (left) and six-fold bond orientation angles  $\alpha_j$  (right) in Eq.(10) for small impurities with  $\zeta = 0.5$  (top) and 1 (bottom) at  $T = 0.05$  in double glass. Heterogeneities become finer with increasing  $\zeta$ .

### III. NUMERICAL RESULTS

If  $c \ll 1$ , our system forms an orientationally disordered crystal (plastic solid) below a certain  $T$ . It then undergoes an orientational phase transition with further lowering  $T$ . In this paper, we add small isotropic impurities as specified in Eq.(9). Since the size ratio  $\sigma_2/\sigma_1$  is rather small, the positions can be highly disordered as well as the orientations, resulting in double glass at low  $T$ . If the size ratio is close to unity, we obtain orientational glass at low  $T$  with increasing  $c$ [18].

#### A. Orientational and positional configurations

In Fig.1, we display snapshots of the particle angles and positions at  $T = 0.05$ , where the thermal fluctuations are very weak. In the left, we do not distinguish  $\theta_j$  and  $\theta_j \pm \pi$ , so depicted are  $[\theta_j]_\pi = \theta_j - p\pi$  in the range  $[0, \pi]$  with an integer  $p$ . In the right, depicted are the sixfold bond angles  $\alpha_j$  in the range  $[0, \pi/3]$  defined by [23, 34]

$$\sum_{k \in \text{bonded}} \exp[6i\theta_{jk}] \propto \exp[6i\alpha_j], \quad (10)$$

where  $\theta_{jk}$  is the angle between  $\mathbf{r}_{kj} = \mathbf{r}_k - \mathbf{r}_j$  and the (horizontal)  $x$  axis, the summation is over the particles

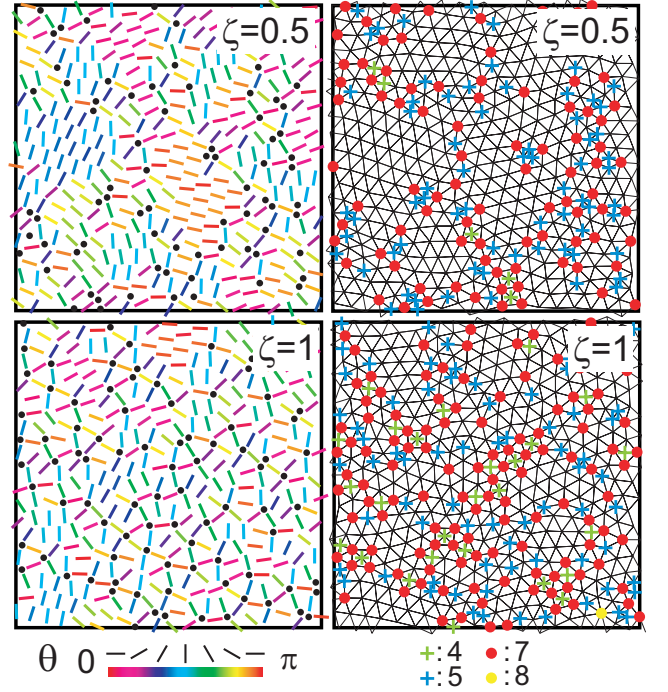


FIG. 2. (Color online) Left: Expanded snapshots of orientational angles  $\theta_j$  around small impurities in the box regions in the left panels of Fig.1. Anchoring is homeotropic and impurity clustering is suppressed with increasing  $\zeta$ . Right: Delaunay diagrams, where marked are the particles with surrounding triangles different from six ( $k \neq 6$ ). Those with  $k = 7$  and 8 are mostly ellipses, while those with  $k = 4$  and 5 are mostly impurities. Here, 70% impurities have  $k = 5$  (fivefold anchoring).

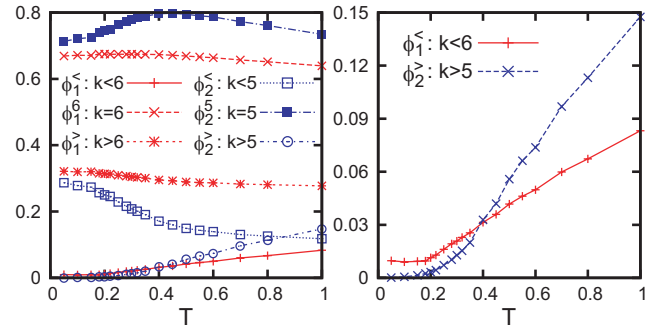


FIG. 3. (Color online) Left: Fractions  $\phi_1^>$ ,  $\phi_1^6$ , and  $\phi_1^<$  of the ellipses with  $k > 6$ ,  $k = 6$ , and  $k < 6$ , respectively, and those  $\phi_2^>$ ,  $\phi_2^5$ , and  $\phi_2^<$  of the impurities with  $k > 5$ ,  $k = 5$ , and  $k < 5$ , respectively, as functions of  $T$  with  $\zeta = 1$ , where  $k$  is the number of the surrounding triangles in the Delaunay diagrams. Here,  $\phi_1^6$ ,  $\phi_1^>$ ,  $\phi_2^<$ , and  $\phi_2^5$  are large at any  $T$ , but  $\phi_1^<$  and  $\phi_2^>$  decrease at low  $T$ . Right: Fractions  $\phi_1^<$  and  $\phi_2^>$  vs  $T$ , which are the fractions of liquidlike defects [35] decreasing at low  $T$ .

$k$  within the range  $|\mathbf{r}_{jk}| < 1.5\sigma_{\alpha\beta}$  (bonded to  $j$ ), and  $6\alpha_j$  is the phase angle of the left hand side. For  $\zeta = 0.5$  we can see small orientationally ordered domains in the left and small polycrystal grains in the right. For  $\zeta = 1$  both the orientations and positions are more disordered, resulting in smaller domains and grains. We remark that increasing the impurity concentration  $c$  from zero also gives rise to smaller domains and grains [18, 23]. Previously, similar mesoscopic patterns of the orientations and the positions were numerically realized in glassy states in the Shintani-Tanaka model [24].

The left panels of Fig.2 display expanded snapshots of  $\theta_j$  for  $\zeta = 0.5$  and 1, where anchoring is homeotropic (perpendicular to the impurity surfaces) [22]. Here, the impurity clustering is significant, which took place during solidification [18]. However, with increasing  $\zeta$ , the impurities are more strongly anchored by the surrounding ellipses and the aggregation of these *solvated* impurities is more suppressed. Similar homeotropic anchoring occurs in water around small ions as hydration due to the ion-dipole interaction [19], which breaks tetrahedral order resulting in vitrification at low  $T$  [20].

In the right panels of Fig.2, we show the Delaunay triangulations of the particle configurations in the left, which are the dual graphs of the Voronoi diagrams. Here, each particle is surrounded by several triangles, so let  $k$  be the number of these triangles, which has the meaning of the coordination number. For a hexagonal lattice, we have  $k = 6$ . Thus, in these panels, we mark the noncrystalline particles with  $k \neq 6$ , where those with  $k = 7$  or 8 are mostly ellipses and those with  $k = 4$  or 5 are impurities. For  $c = 0.2$ , a majority of the ellipses ( $\sim 65\%$ ) have  $k = 6$  in the presence of a considerable fraction of small crystalline regions, while a majority of the impurities ( $\sim 70\%$ ) have  $k = 5$  due to the homeotropic anchoring of the surrounding ellipses.

In the left panel of Fig.3, we display the fractions of the ellipses with  $k > 6$ ,  $k = 6$ , and  $k < 6$  and those of the impurities with  $k > 5$ ,  $k = 5$ , and  $k < 5$ . These six fractions are denoted by  $\phi_1^>$ ,  $\phi_1^6$ ,  $\phi_1^<$ ,  $\phi_2^>$ ,  $\phi_2^5$ , and  $\phi_2^<$ , respectively, as functions of  $T$ . At low  $T$ ,  $k$  is mostly 6 or 7 for the ellipses and is mostly 4 or 5 for the impurities. In fact, for the data in Figs.1 and 2 at  $T = 0.05$ , we have  $(\phi_1^6, \phi_1^>) \cong (0.66, 0.33)$  and  $(\phi_2^<, \phi_2^5) \cong (0.28, 0.71)$  for  $\zeta = 1$ , while these sets are  $(0.73, 0.26)$  and  $(0.05, 0.94)$ , respectively, for  $\zeta = 0.5$ . In the right panel of Fig.3,  $\phi_1^<$  and  $\phi_2^<$  are very small at low  $T$  and increase with increasing  $T$ . Thus, the ellipses with  $k < 6$  and the impurities with  $k > 5$  represent liquidlike defects [35].

Hentschel *et al.* [35] studied the positional disorder using the Voronoi graphs for a mixture of circular particles with the soft-core potential in two dimensions. In their simulation, small (large) particles enclosed by heptagons (pentagons) form liquidlike defects decreasing at low  $T$ .

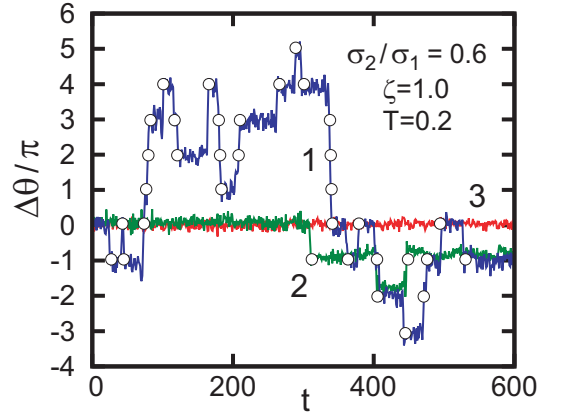


FIG. 4. (Color online) Time-evolution of angle changes  $\Delta\theta_i(t_0, t_0 + t)$  in Eq.(11) for (1) a frequently flipping ellipse, (2) an infrequently flipping one, and (3) an inactive one for  $\zeta = 1$  and  $T = 0.1$ . Flip events occur at points ( $\circ$ ) on the curves (see the appendix). These jumps are very different from thermal vibrations but occur thermally.

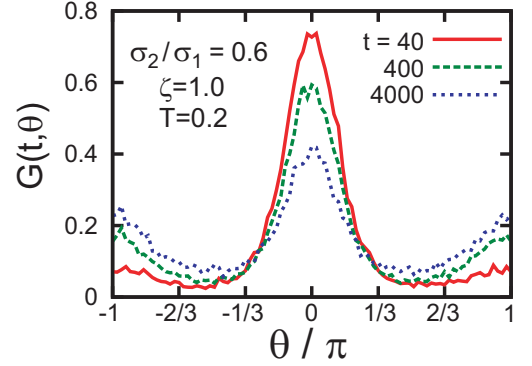


FIG. 5. (Color online) Time-dependent angle distribution function  $G(t, \theta)$  in Eq.(12) at  $t = 40, 400$ , and  $4000$  for  $\zeta = 1$  and  $T = 0.2$ . Peaks emerge at  $\theta = \pm\pi$  due to flip motions on the time scale of  $\tau_1 = 400$ . Afterwards,  $G(t, \theta) \rightarrow 1/2\pi$  on the time scale of  $\tau_2 = 24000$ .

## B. Time-correlation functions

For strong short-range anchoring, the rotational dynamics sensitively depends on whether the anisotropic particles are close or far from the impurities. In Fig.4, we show time-evolution of the angle changes,

$$\Delta\theta_i(t_0, t + t_0) = \theta_i(t + t_0) - \theta_i(t_0), \quad (11)$$

where we pick up a rapidly rotating ellipse, a rarely flipping one, and an inactive one. We can see instantaneous flip motions by  $\pm\pi$ . In previous simulations in glassy states, they observed flips for rod-like molecules [10, 13, 14] and large angle jumps for ortho-terphenyl (OTP) [11, 12].



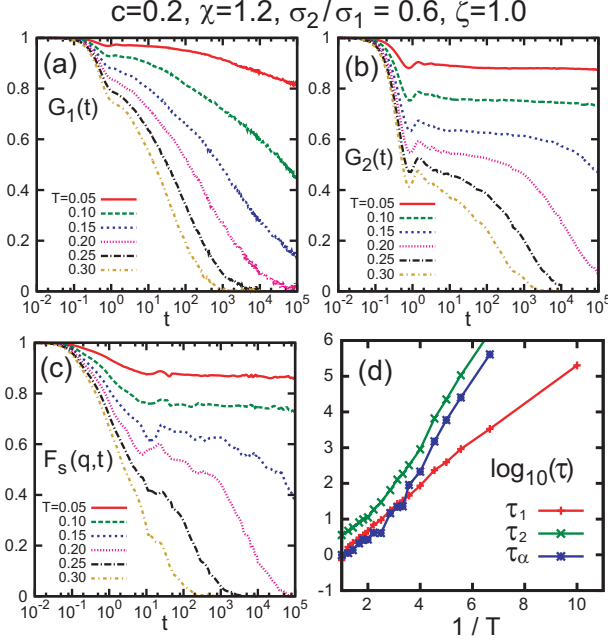


FIG. 6. (Color online) (a)  $G_1(t)$ , (b)  $G_2(t)$ , (c)  $F_s(q, t)$  at  $q = 2\pi$  for ellipses at six  $T$ . (d) Relaxation times  $\tau_1$ ,  $\tau_2$ , and  $\tau_\alpha$  in Eqs.(14)-(16) vs  $1/T$ . Here,  $\zeta = 1$  and time  $t$  is in units of  $\tau_0$  in Eq.(8).

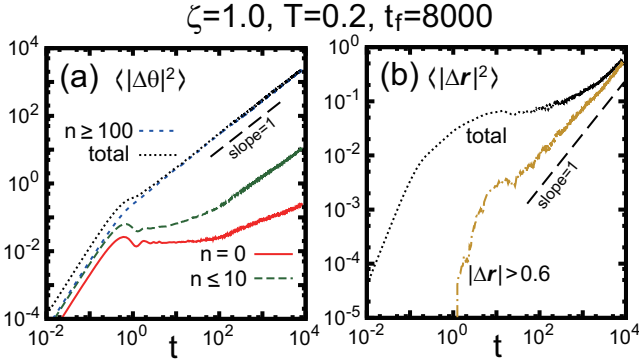


FIG. 7. (Color online) Angular and positional mean-square displacements for  $\zeta = 1$  and  $T = 0.2$ . (a) Angular one  $M_\theta(t)$  in Eq.(17) and contributions from those with  $n_i \geq 100$ ,  $n_i \leq 10$ , and  $n_i = 0$ , where  $n_i$  is the flip number for  $t_f = 20\tau_1 = 8000$  (see the appendix). The contribution from  $n_i \geq 100$  approaches  $M_\theta(t)$  for  $t \gtrsim 1$ , leading to  $D_R = 0.14$ . (b) Positional one  $M(t)$  in Eq.(18) and contribution from those with  $\Delta r_i > 0.6$  in Eq.(21), where the latter grows linearly for  $t \gtrsim 20$  with  $D = 1.4 \times 10^{-5}$ .

We introduce the distribution of the angle changes,

$$G(t, \theta) = \frac{1}{N_1} \sum_{i \in 1} \langle \delta([\Delta\theta_i(t)]_{2\pi} - \theta) \rangle, \quad (12)$$

where  $\Delta\theta_i(t) = \Delta\theta_i(t_0, t + t_0)$  and  $-\pi \leq \theta < \pi$ . For any angle  $\varphi$ , we define  $[\varphi]_{2\pi} = \varphi - 2p\pi$ , which is in the range

$[-\pi, \pi]$  with an integer  $p$ . Furthermore, we consider the  $\ell$ -th moments of  $G(t, \theta)$  given by

$$\begin{aligned} G_\ell(t) &= \int_{-\pi}^{\pi} d\theta G(t, \theta) \cos(\ell\theta) \\ &= \frac{1}{N_1} \sum_{i \in 1} \langle \cos[\ell\Delta\theta_i(t)] \rangle. \end{aligned} \quad (13)$$

We calculated  $G(t, \theta)$ ,  $G_1(t)$ , and  $G_2(t)$  by taking the average  $\langle \dots \rangle$  over the initial time  $t_0$  and over five runs.

In Fig.5, we show time-evolution of  $G(t, \theta)$ , where flip motions give rise to peaks at  $\theta = \pm\pi$  growing on the time scale of  $\tau_1$ . Thus, these flip motions cause the decay of  $G_1(t)$  in Fig.6(a). However,  $G_2(t)$  is unchanged by the turnovers and decays more slowly after the initial relaxation in Fig.6(b). Notice that  $G(t, \theta)$  tends to  $1/2\pi$  on the time scale of  $\tau_2$ . In Fig.6(c), we also show the self part of the density time-correlation function  $F_s(q, t)$  at  $q = 2\pi$  for the ellipses, which closely resembles  $G_2(t)$ .

We define the relaxation times  $\tau_1$ ,  $\tau_2$ , and  $\tau_\alpha$  as

$$G_1(\tau_1) = 1/e, \quad (14)$$

$$G_2(t) \propto \exp[-(t/\tau_2)^\beta] \quad (t > 1), \quad (15)$$

$$F_s(q, t) \propto \exp[-(t/\tau_\alpha)^\gamma] \quad (t > 1), \quad (16)$$

where the exponents  $\beta$  and  $\gamma$  are about 0.4 for  $T \lesssim 0.2$ . We here determine  $\tau_2$  and  $\tau_\alpha$  from the long-time relaxations of  $G_2(t)$  and  $F_s(q, t)$ , respectively. In Fig.6(d), we plot them, where  $\tau_1 \ll \tau_\alpha \sim \tau_2$ . In all the  $T$  range in Fig.6(d),  $\tau_1$  may be nicely fitted to the Arrhenius form,  $\ln(\tau_1) = 1.4/T - 1.2$ . On the other hand,  $\tau_2$  and  $\tau_\alpha$  exhibit a changeover at  $T \sim 0.2$  and can be fitted to the Arrhenius forms as  $\ln(\tau_2) = 2.6/T - 3.0$  and  $\ln(\tau_\alpha) = 2.6/T - 4.5$ , for  $T \lesssim 0.2$ , so  $\tau_2/\tau_\alpha \cong 4$  for  $T \lesssim 0.2$ . Thus,  $G_1(t)$  decays mainly due to thermally activated flip motions, which are nearly decoupled from the translational motions. On the other hand,  $G_2(t)$  and  $F_s(q, t)$  decay at longer times due to irreversible configuration changes involving at least several particles.

In three dimensions, the distribution of the angles  $\cos^{-1}[\mathbf{n}_i(t_0 + t) \cdot \mathbf{n}_i(t_0)]$  was calculated for OTP [11] and for dumbbells [13, 14]. In these papers, this distribution exhibited peaks due to orientational jumps. Also in the rotational time-correlation functions in three dimensions, the Legendre polynomials  $P_\ell(u_i(t))$  with  $u_i(t) = \mathbf{n}_i(t_0 + t) \cdot \mathbf{n}_i(t_0)$  were used [10, 12–17], where  $G_\ell(t)$  with even  $\ell$  decayed slower than those with odd  $\ell$  at low  $T$ . These previous findings are in accord with our results.

### C. Mean-square displacements

In the literature, the angular mean-square displacement has been calculated to study the rotational diffusion [12–15, 17]. In two dimensions, it is defined by

$$M_\theta(t) = \langle |\Delta\theta|^2 \rangle = \frac{1}{N_1} \sum_{i \in 1} \langle |\Delta\theta_i(t_0, t_0 + t)|^2 \rangle. \quad (17)$$

We also introduce the usual positional mean-square displacement for the ellipses by

$$M(t) = \langle |\Delta \mathbf{r}|^2 \rangle = \frac{1}{N_1} \sum_{i \in 1} \langle |\Delta \mathbf{r}_i(t_0, t_0 + t)|^2 \rangle, \quad (18)$$

where  $\Delta \mathbf{r}_i(t_0, t_0 + t) = \mathbf{r}_i(t_0 + t) - \mathbf{r}_i(t_0)$ . At very short times, these quantities exhibit the ballistic behavior ( $\propto t^2$ ). At long times, they grow linearly in time as

$$M_\theta(t) \cong 2D_R t, \quad (19)$$

$$M(t) \cong 4Dt, \quad (20)$$

where  $D_R$  and  $D$  are the rotational and translational diffusion constants, respectively. If the rotational activity is strongly heterogeneous, the so-called Stokes-Einstein-Debye relation  $D_R \sim k_B T / \eta a$  does not hold [3, 12], where  $\eta$  is the viscosity and  $a$  is the radius of the diffusing particle. In our case,  $M_\theta(t)$  is greatly increased by rapidly flipping ellipses and  $D_R$  from it does not correspond to any experimentally observed relaxation times at low  $T$ .

In Fig.7(a), we plot  $M_\theta(t)$  for  $\zeta = 1$  and  $T = 0.2$ . Here, it attains the diffusion behavior with  $D_R = 0.14$  for  $t \gtrsim 1$ , while  $G_1(t)$  decays slower with  $\tau_1 = 400$ . We also display the contributions to the sum in  $M_\theta(t)$  in Eq.(17) from the ellipses with  $n_i = 0$ ,  $n_i \leq 10$ , and  $n_i \geq 100$ , where  $n_i$  is the flip number of ellipse  $i$  in a time interval with width  $t_f = 8000$  (see the appendix). The fractions of these three groups are 0.16, 0.34, and 0.39, respectively. Remarkably, the contribution from  $n_i \geq 100$  approaches  $M_\theta(t)$  for  $t \gtrsim 1$ , while that from  $n_i \leq 10$  behaves diffusively as  $0.7 \times 10^{-3} \times 2t$  for  $t \gtrsim \tau_1$ . Thus, the effective rotational diffusion constant of the ellipses with  $n \leq 10$  is  $0.7 \times 10^{-3} / 0.34 = 2 \times 10^{-3}$ . The  $M_\theta(t)$  itself exhibits the plateau behavior at much lower temperatures (say,  $T = 0.05$ ), while the contributions from  $n = 0$  and  $n \leq 10$  exhibit it at  $T = 0.2$ .

In Fig.7(b), for  $\zeta = 1$  and  $T = 0.2$ ,  $M(t)$  still in the course of plateau-to-diffusion crossover even at  $t = 10^4$ . To obtain small  $D$ , we also plot the contribution from the ellipses with large displacements [36],

$$M^>(t) = \frac{1}{N_1} \sum_{i \in 1} \langle \Theta(\Delta \mathbf{r}_i(t) - \ell_c) |\Delta \mathbf{r}_i(t)|^2 \rangle, \quad (21)$$

where  $\Delta \mathbf{r}_i(t)$  is an abbreviation of  $|\Delta \mathbf{r}_i(t_0, t_0 + t)|$  and  $\Theta(u)$  is the step function being equal to 1 for  $u \geq 0$  and to 0 for  $u < 0$ . The threshold length  $\ell_c$  is set equal to 0.6. In this restricted sum, the thermal vibrational motions within transient cages are excluded, so it picks up the thermally activated jumps only. As a result, we have the linear growth  $M^>(t) \cong 4Dt$  with  $D = 1.4 \times 10^{-5} \sim 10^{-4} D_R$  from the early stage  $t \gtrsim 20$ . This behavior of  $M^>(t)$  is insensitive to a small change of  $\ell_c$  [36]. For example, almost the same results followed for  $\ell_c = 0.8$ .

As a similar observation, Chong and Kob found that  $D_R \tau_2$  grows strongly with lowering  $T$  for a mixture of rigid dumbbell molecules [17]. See more discussions for other molecular systems in the item (i) in the summary.

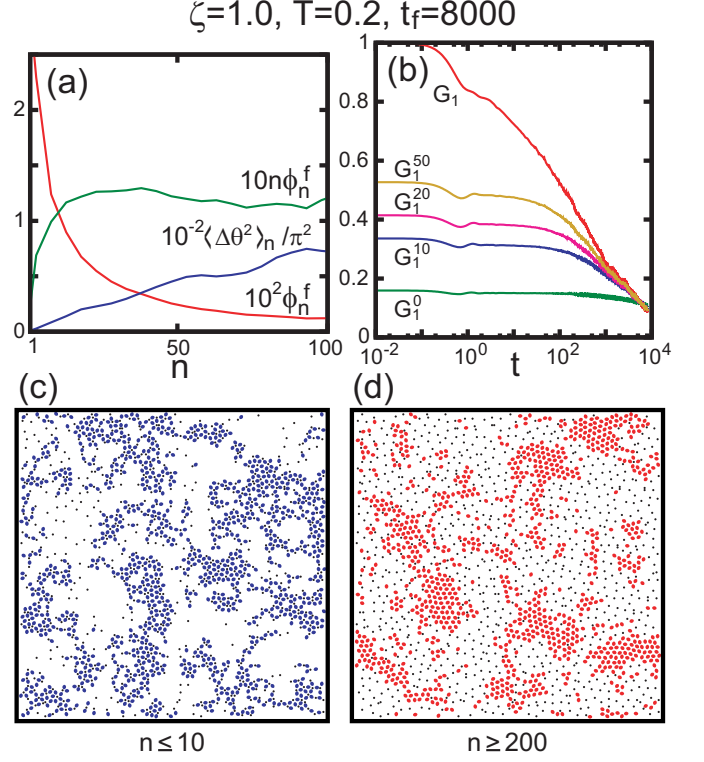


FIG. 8. (Color online) (a)  $10^2 \phi_n^f$ ,  $10n \phi_n^f$  for  $n \geq 1$ , and  $10^{-2} \langle |\Delta \theta|^2 \rangle_n / \pi^2$  in Eq.(23), where  $t_f = 20\tau_1 = 8000$  (averages over six runs). (b)  $G_1(t)$  in Eq.(13) and  $G_1^n(t)$  in Eq.(28) with  $n = 0, 10, 20$ , and  $50$  at  $t = t_f$ , where the latter approach the former at long times. Snapshots of ellipses with  $n_i \leq 10$  in (c) and those with  $n_i \geq 200$  in (d), whose heterogeneities are correlated with the impurity clustering.

#### D. Distribution of flip numbers

The large size of  $D_R$  is due to the presence of ellipses frequently undergoing flip motions. In the appendix, we will give a method of determining the flip number  $n_i$  for each ellipse  $i$  in a time interval  $[t_0, t_0 + t_f]$ . We should choose a sufficiently large width  $t_f$  to detect a wide range of  $n_i$ . In the following,  $t_f = 8000$  at  $T = 0.2$  in Figs.7 and 8 and  $t_f = 10^5$  at  $T = 0.05$  in Fig.9. The curves in Figs.8(a), 8(b), and 9(a) are the averages over six runs.

For a given time interval  $[t_0, t_0 + t_f]$ , the fraction of the ellipses with  $n$  flips is written as

$$\phi_n^f = \sum_{i \in 1} \langle \delta_{nn_i} \rangle / N_1. \quad (22)$$

We further introduce the  $n$ -dependent mean-square displacement among the ellipses with  $n$  flips as

$$\langle |\Delta \theta|^2 \rangle_n(t) = \frac{1}{N_1 \phi_n^f} \sum_{i \in 1} \langle \delta_{nn_i} |\Delta \theta_i(t_0, t_0 + t)|^2 \rangle. \quad (23)$$

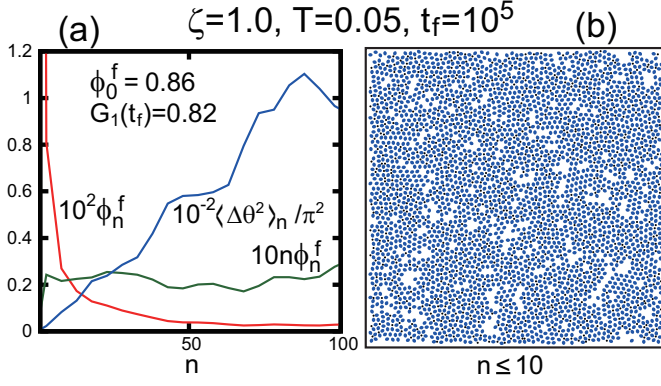


FIG. 9. (Color online)  $10^2 \phi_n^f$ ,  $10n \phi_n^f$ , and  $10^{-2} \langle |\Delta \theta|^2 \rangle_n / \pi^2$  (averages over six runs) in (a) and snapshot of ellipses with  $n \leq 10$  in (b), where  $\zeta = 1$ ,  $T = 0.05$ , and  $t_f = 10^5$ . At this low  $T$ ,  $\phi_0^f = 0.86$  and the fraction of the depicted ellipses in (b) is 0.92.

It follows the sum relation,

$$M_\theta(t) = \sum_{n \geq 0} \phi_n^f \langle |\Delta \theta|^2 \rangle_n(t). \quad (24)$$

In our case, most ellipses undergo  $+\pi$  flips and  $-\pi$  flips equally on long times, so  $\sum_{i \in 1} \langle \delta_{nn_i} \Delta \theta_i(t_0, t_0 + t) \rangle = 0$ .

In Fig.8(a), we plot  $\phi_n^f$ ,  $n \phi_n^f$ , and  $\langle |\Delta \theta|^2 \rangle_n(t_f)$  (where  $t = t_f$ ) for  $\zeta = 1$  and  $T = 0.2$ . Here, the fraction of the ellipses with no flip is given by  $\phi_0^f = 0.16$ . We find that the flip number distribution is very broad as

$$\phi_n^f \sim 0.1 n^{-1}, \quad (25)$$

in the range  $1 \ll n < n_{\max}$ , where  $n_{\max}$  is an upper bound about  $10^3$ . In the present case, the sums of  $\phi_n^f$  in the ranges  $1 \leq n \leq 10$ ,  $11 \leq n \leq 99$ , and  $n \geq 100$  are 0.18, 0.27, and 0.39, respectively. Furthermore, we find

$$\langle |\Delta \theta|^2 \rangle_n(t) \sim \pi^2 n_t = \pi^2 n t / t_f \quad (26)$$

for  $t \gg 1$  and  $n \gg 1$ . In a general time width  $t$ , the ellipses with  $n$  flips in the reference time width  $t_f$  should flip  $n_t = n t / t_f$  times on the average, where  $t \gg 1$  and  $n \gg 1$ . Then, together with the sentence below Eq.(24), Eq.(26) is a natural relation. From Eqs.(24)-(26) we find

$$D_R \sim n_{\max} / t_f, \quad (27)$$

which means that  $D_R$  is determined by rapidly rotating ellipses. To be self-consistent,  $n_{\max}$  should be proportional to  $t_f$ ; then,  $D_R$  is independent of  $t_f$ .

In Fig.8(b), we compare  $G_1(t)$  and the restricted sums,

$$G_1^n(t) = \frac{1}{N_1} \sum_{i \in 1} \left\langle \Theta(n - n_i) \cos[\Delta \theta_i(t_0, t_0 + t)] \right\rangle, \quad (28)$$

where we set  $n = 0, 10, 20$ , and 50. We here pick up the ellipses with flip numbers not exceeding  $n$  owing to the

step function  $\Theta$ . We can see that these  $G_1^n(t)$  are nearly constant for some time and become nearly equal to  $G_1(t)$  after long times. For  $t \gtrsim 10^3$ ,  $G_1(t)$  is composed of the contributions from the ellipses with  $n \leq 10$ .

In Figs.8(c) and (d), we show snapshots of the ellipses with  $n \leq 10$  and  $n \geq 200$ , respectively. The distributions of these rotationally inactive and active ellipses are highly heterogeneous. This marked feature is rather natural in view of the mild aspect ratio 1.23 and the significant impurity clustering. In fact, the impurities are nearly absent in the red regions in Fig.8(b).

In Fig.9, we also show that the flip motions still remain even at  $T = 0.05$ . In this case, we find  $G_1(t) \sim 0.8$  at  $t = 10^5$  in Fig.6(a), but we estimate  $\tau_1 \sim 10^{12}$  from the extrapolation of the Arrhenius form (see the sentences below Eq.(16)). In Fig.9(a), we find  $\phi_0^f = 0.86$  and  $\phi_n^f \sim 0.02 n^{-1}$  and again obtain Eq.(26) for  $\zeta = 1$ ,  $T = 0.05$ , and  $t_f = 10^5$ . In Fig.9(b), displayed is a snapshot of the ellipses with  $n_i \leq 10$ , whose fraction is  $\sum_{n \leq 10} \phi_n^f = 0.92$ . Even at this low  $T$ , 2% ellipses have  $n_i > 200$ . We have  $D_R = 1.2 \times 10^{-3}$  due to these rapidly flipping ellipses. This snapshot was produced by the initial particle configuration common to that in Fig.8(b). Most of the ellipses in the red regions in Fig.8(b) are now inactive, since their orientation alignment increases with lowering  $T$ .

### E. Dynamic heterogeneities in non-flip rotations and displacements

Now, we examine the long-time structural relaxation caused by collective configuration changes, where large displacements induce large non-flip rotations. These events should occur repeated in the same fragile regions on time scales longer than  $\tau_2$  [29, 36].

In Fig.10, we illustrate time-development of a configuration change at successive times  $t_0 + t$  with  $0 \leq t \leq 10$ . Depicted are the ellipses with  $\Delta r_i(t) = |\Delta \mathbf{r}_i(t_0, t_0 + t)| > 0.6$  or  $c_i(t) < 0.2$ , where

$$c_i(t) = \cos[2\Delta \theta_i(t_0, t_0 + t)]. \quad (29)$$

The condition  $c_i(t) < 0.2$  means  $0.22\pi < |\Delta \theta_i(t_0, t_0 + t)| < 0.78\pi$  in the range  $[-\pi, \pi]$ . From Eq.(13) we have  $G_2(t) = \sum_{i \in 1} \langle c_i(t) \rangle / N_1$ . In the narrow region in Fig.10, the particle configuration was nearly stationary for  $t \leq 0$ , but large particle motions started for  $t > 0$  and continued on a time scale of 10. We can see circulating particle motions at  $t = 6$  and 8 and stringlike ones at  $t = 10$  [27–29, 36]. The orientations of these ellipses are largely changing with their movements. For  $t > 10$ , the subsequent displacements became small, but considerable orientational motions persisted until  $t \sim 20$ .

We examine the non-flip motions in terms of  $c_i(t)$  in Eq.(29), since it is invariant with respect to turnovers. In Fig.11(a), we visualize the correlation between  $c_i(t)$  and  $\Delta r_i(t) = \Delta r_i(t)$  for  $\zeta = 1$  and  $T = 0.2$ . We set

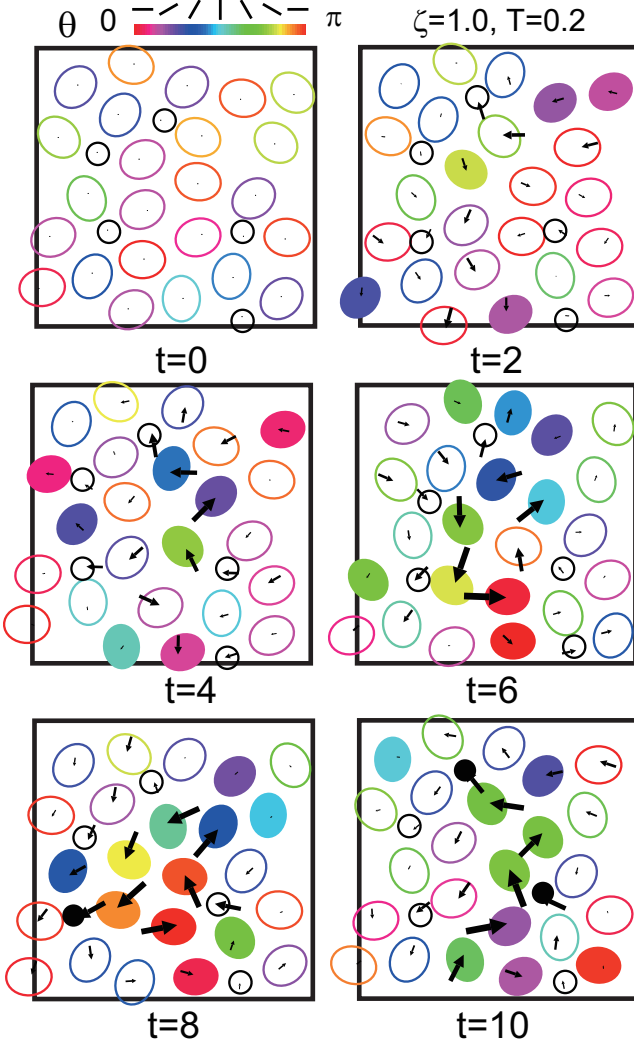


FIG. 10. (Color online) Time-development of a configuration change at successive times  $t_0 + t$  with  $t = 0, 2, 4, 6, 8$ , and  $10$  for  $\zeta = 1$  and  $T = 0.2$ . Ellipses with  $|\Delta \mathbf{r}_i(t_0, t_0 + t)| > 0.6$  or  $c_i = \cos(2|\Delta \theta(t_0, t_0 + t)|) < 0.2$  are written. Arrows represent  $\Delta \mathbf{r}_i(t_0, t_0 + t)$  and colors  $\theta_i(t_0 + t)$  according to the color bar as in Fig.1. Impurities with  $|\Delta \mathbf{r}_i(t_0, t_0 + t)| > 0.6$  are written as black circles ( $\bullet$ ). Other particles are written as white ellipses or circles.

$t = t_f = 8000$ , which is one-third of  $\tau_2 \sim 24000$  ( $\sim 4\tau_\alpha$ ). We present a snapshot of the ellipses with (a)  $c_i < 0.2$  and  $\Delta r_i > 0.6$ , (b)  $c_i < 0.2$  and  $\Delta r_i < 0.6$ , and (c)  $c_i > 0.2$  and  $\Delta r_i > 0.6$ . Here, we exclude the ellipses with  $n_i > 200$  ( $\sim 30\%$ ), because they do not exhibit the glassy behavior. The fractions of these depicted groups are (a) 0.08, (b) 0.10, and (c) 0.09, while the fraction of the ellipses with  $c_i > 0.2$ ,  $\Delta r_i < 0.6$ , and  $n_i \leq 200$  is 0.41. Thus, if we consider the ellipses with  $c_i < 0.2$  and  $n_i < 200$ , a half of them have undergone displacements with  $\Delta r_i > 0.6$ . Also, if we consider the ellipses with  $\Delta r_i > 0.6$  and  $n_i < 200$ , a half of them have undergone large angle changes with  $c_i < 0.2$ .

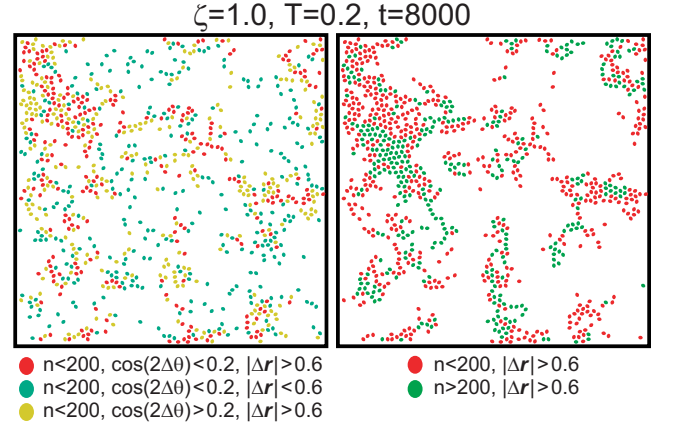


FIG. 11. (Color online) Comparison of ellipses with  $c_i \equiv \cos[2\Delta \theta_i(t_0, t_0 + t)] < 0.2$  and particles with large displacement  $\Delta r_i \equiv |\Delta \mathbf{r}_i(t_0, t_0 + t)| > 0.6$  for  $\zeta = 1$  and  $T = 0.2$  at  $t = t_f = 8000$ . In the left, depicted are three groups of ellipses with  $c_i < 0.2$  and  $\Delta r_i > 0.6$  (in red),  $c_i < 0.2$  and  $\Delta r_i < 0.6$  (in green),  $c_i > 0.2$  and  $\Delta r_i > 0.6$  (in yellow), whose fractions are 0.08, 0.10, and 0.09, respectively. In the right, depicted are  $0.18N_1$  ellipses with  $\Delta r_i > 0.6$  and  $n_i < 200$  (in red) and  $0.11N_1$  ones with  $\Delta r_i > 0.6$  and  $n_i > 200$  (in green).

In Fig.11(b), displayed is a snapshot of the ellipses with (a)  $\Delta r_i > 0.6$  and  $n_i < 200$  (18%) and (b)  $\Delta r_i > 0.6$  and  $n_i > 200$  (11%). The group (a) here consists of the groups (a) and (b) in Fig.11(a). Here, the ellipses in these two groups form clusters, indicating collective displacements. In addition, clusters of one group are adjacent to those of another group. Thus, rotationally active ellipses with large  $n_i$  tend to be translationally active also.

#### IV. SUMMARY AND REMARKS

We have performed simulation of a mixture of elliptic particle with a mild aspect ratio ( $= 1.23$ ) and smaller circular impurities with  $\sigma_2/\sigma_1 = 0.6$  at 20%. We have assumed an angle-dependent attractive interaction between the ellipses and the impurities ( $\propto \zeta$ ), which leads to the homeotropic anchoring of the ellipses around each impurity. We summarize our main simulation results.

1) We have shown snapshots of the orientations and the positions in Figs.1 and 2, which are mesoscopically heterogeneous. From the Delaunay triangulation in the right panels of Fig.2, we have found that the number of surrounding triangles (the coordination number) is 6 or 7 for the ellipses and 5 or 4 for the impurities in glassy states, as plotted in Fig.3. A majority of the impurities ( $\sim 70\%$ ) are surrounded by 5 ellipses, analogously to the case of the Shintani-Tanaka model[24].

2) We have calculated the distribution function of the angle changes  $G(t, \theta)$  in Eq.(12), which exhibits peaks at  $\theta = \pm\pi$  for large  $t$  due to flip motions as in Fig.5. We have found that the rotational time-correlation functions



$G_1(t)$  and  $G_2(t)$  of the ellipses relax very differently at long times in Fig.6, because  $G_1(t)$  decays due to flip motions and  $G_2(t)$  due to configuration changes.

3) We have found that the angular mean-square displacement  $M_\theta(t)$  in Eq.(17) behaves as  $2D_R t$  rapidly for  $t \gtrsim 1$  with very large  $D_R$  in Fig.7. This is in marked contrast to the slow time-evolution of the translational mean-square displacement  $M(t)$ . However, the contribution to  $M(t)$  from the largely displaced ellipses ( $|\Delta r_i| > 0.6$ ) has exhibited the diffusion behavior with  $D = 10^{-4}D_R$ , because the diffusion is governed by the activation dynamics [36].

4) We have displayed the fractions  $\phi_n^f$  of the ellipses with  $n$  flips in a time interval  $[t_0, t_0 + t_f]$ , where  $t_f = 8000$  at  $T = 0.2$  in Figs.7 and 8 and  $t_f = 10^5$  at  $T = 0.05$  in Fig.9. We have found a very broad distribution  $\phi_n^f (\propto n^{-1})$  for  $1 \ll n < n_{\max}$ . The angular mean-square displacement  $\langle |\Delta \theta|^2 \rangle_n(t)$  among the ellipses with  $n$  flips behaves as  $\pi^2 n t / t_f$ . Then  $D_R \sim n_{\max} / t_f$  due to rapidly flipping ellipses. We have also shown that the long-time decay of  $G_1(t)$  is determined by ellipses with  $n \leq 10$  in Fig.8(b).

5) The distributions of the rotationally inactive ( $n \leq 10$ ) and active ( $n \geq 200$ ) ellipses at  $T = 0.2$  have been presented in Figs.8(c) and (d), while that of the inactive ones at  $T = 0.05$  has been given in Fig.9(b).

6) We have illustrated time-development of a configuration change in Fig.10, where large displacements and non-flip rotations are coupled. We have demonstrated close correlation between non-flip rotations and large displacements in Fig.11.

We make remarks as follows.

(i) Our potential energy is invariant with respect to turnovers. This is also the case of diatomic molecules or dumbbells [16, 17], for which the flip motions should be highly heterogeneous for mild aspect ratios. For methanol, Sindzingre and Klein [10] found flip motions near the glass transition. For OTP, Lewis and Wahnström [11] found translation-free orientational jumps, while Lombardo *et al.* [12] found an enhancement in the rotational motions relative to the translation motions at low  $T$ . For these systems, the heterogeneity of orientational jumps should be examined in more detail.

(ii) We have chosen a mild aspect ratio ( $= 1.23$ ) to find significant flip motions. However, an increase in the aspect ratio leads to a decrease in the flip frequency, on which we will report shortly.

(iii) We have suppressed the clustering of small impurities by the angle-dependent attractive interaction. If we consider large impurities (say,  $\sigma_2/\sigma_1 = 1.4$ ), we may realize double glass by adding a repulsive interaction among the impurities suppressing crystal formation.

(iv) The phase behavior of mixtures of two species of anisotropic particles should be studied in future, where we expect nematic or smectic glass.

(v) The spatial scales of the structural heterogeneities depend on various parameters. If the oriented domains are not too small, there arises a large orientation-strain coupling, leading to soft elasticity and a shape-memory effect [18]. These effects were observed for Ti-Ni alloys [37] (where atomic displacements within unit cells cause structural changes). When anisotropic particles have electric dipoles[7], mesoscopic polar domains appear as in ferroelectric glass (relaxors) [38]. Including such metallic alloys also, we point out relevance of the compositional heterogeneity in the development of mesoscopic order.

## ACKNOWLEDGMENTS

This work was supported by Grant-in-Aid for Scientific Research from the Ministry of Education, Culture, Sports, Science and Technology of Japan. K. T. was supported by the Japan Society for Promotion of Science. The present numerical calculations were carried out on SR16000 at YITP in Kyoto University.

## Appendix: Flip events in numerical analysis

In our numerical analysis, we determine a series of flip times,  $t_{i1}, t_{i2}, t_{i3}, \dots$  for each ellipse  $i$ . We write the angle change as  $\Delta \theta_i(t) = \Delta \theta_i(t_0, t + t_0)$ , suppressing  $t_0$ . (i) At the first flip time  $t_{i1}$  we set

$$|\Delta \theta_i(t_{i1})| = 2\pi/3. \quad (\text{A1})$$

For  $t > t_{i1}$  we introduce

$$\Delta \theta_{i1}(t) = \Delta \theta_i(t) \pm \pi, \quad (\text{A2})$$

where  $+\pi$  or  $-\pi$  is chosen such that  $|\Delta \theta_{i1}(t_{i1}+0)| < \pi/2$ .

(ii) At the second flip time  $t_{i2}$  we set

$$|\Delta \theta_{i1}(t_{i2})| = 2\pi/3. \quad (\text{A3})$$

For  $t > t_{i2}$  we again introduce

$$\Delta \theta_{i2}(t) = \Delta \theta_{i1}(t) \pm \pi, \quad (\text{A4})$$

where  $+\pi$  or  $-\pi$  is chosen such that  $|\Delta \theta_{i2}(t_{i2}+0)| < \pi/2$ .

(iii) We repeat these procedures to obtain the successive flip times. See Fig.4 for examples of the flip time series.

Note that the threshold  $2\pi/3$  in Eqs.(A1) and (A3) may be changed to another angle, say  $5\pi/6$ . However, the resultant flip time series is rather insensitive to this choice as long as it is in the range  $[\pi/4, \pi/2]$ .

[1] C. A. Angell, K. L. Ngai, G. B. McKenna, P. F. McMillan, and S. W. Martin, *J. Appl. Phys.* **88**, 3113 (2000).

[2] K. Binder and W. Kob, *Glassy Materials and Disordered*

- Solids* (World Scientific, Singapore, 2005).
- [3] F. Fujara, B. Geil, H. Sillescu, and G. Fleischer, *Z. Phys. B* **88**, 195 (1992); M. T. Cicerone and M. D. Ediger, *J. Chem. Phys.* **104**, 7210 (1996).
  - [4] A. Winkler, A. Latz, R. Schilling, and C. Theis, *Phys. Rev. E* **62**, 8004 (2000).
  - [5] S.-H. Chong and W. Götze, *Phys. Rev. E* **65**, 041503 (2002).
  - [6] R. Zhang and K. S. Schweizer, *J. Chem. Phys.* **133**, 104902 (2010); *ibid.* **136**, 154902 (2012).
  - [7] U. T. Höchli, K. Knorr, and A. Loidl, *Adv. Phys.* **39**, 405 (1990).
  - [8] Z. Zheng, F. Wang, and Y. Han, *Phys. Rev. Lett.* **107**, 065702 (2011).
  - [9] C. K. Mishra, A. Rangarajan, and R. Ganapathy, *Phys. Rev. Lett.* **110**, 188301 (2013).
  - [10] P. Sindzingre and M. L. Klein, *J. Chem. Phys.* **96**, 4681 (1992).
  - [11] L. J. Lewis and G. Wahnström, *Phys. Rev. E* **50**, 3865 (1994); *J. Non-Cryst. Solids* **172**, 69 (1994).
  - [12] T. G. Lombardo, P. G. Debenedetti, and F. H. Stillinger, *J. Chem. Phys.* **125**, 174507 (2006).
  - [13] S. Kämmerer, W. Kob, and R. Schilling, *Phys. Rev. E* **56**, 5450 (1997).
  - [14] C. De Michele and D. Leporini, *Phys. Rev. E* **63**, 036702 (2001).
  - [15] S.-H. Chong, A. J. Moreno, F. Sciortino, and W. Kob, *Phys. Rev. Lett.* **94**, 215701 (2005).
  - [16] A. J. Moreno, S.-H. Chong, W. Kob, and F. Sciortino, *J. Chem. Phys.* **123**, 204505 (2005).
  - [17] S.-H. Chong and W. Kob, *Phys. Rev. Lett.* **102**, 025702 (2009).
  - [18] K. Takae and A. Onuki, *EPL* **100**, 16006 (2012).
  - [19] J. N. Israelachvili, *Intermolecular and Surface Forces* (Academic Press, London, 1991).
  - [20] C. A. Angell and E. J. Sare, *J. Chem. Phys.* **49**, 4713 (1968); M. Kobayashi and H. Tanaka, *J. Phys. Chem. B*, **115**, 14077 (2011).
  - [21] G. A. Vliegenthart, A. van Blaaderen, and H. N. W. Lekkerkerker, *Faraday Discuss.* **112**, 173 (1999).
  - [22] D. Antypov and D. J. Cleaver, *J. Chem. Phys.* **120**, 10307 (2004).
  - [23] T. Hamanaka and A. Onuki, *Phys. Rev. E* **74**, 011506 (2006); *ibid.* **75**, 041503 (2007).
  - [24] H. Shintani and H. Tanaka, *Nat. Phys.* **2**, 200 (2006).
  - [25] T. Kawasaki, T. Araki, and H. Tanaka, *Phys. Rev. Lett.* **99**, 215701 (2007).
  - [26] R. Yamamoto and A. Onuki, *J. Phys. Soc. Jpn.* **66**, 2545 (1997); *Phys. Rev. E* **58**, 3515 (1998).
  - [27] C. Donati, J. F. Douglas, W. Kob, S. J. Plimpton, P. H. Poole, and S. C. Glotzer, *Phys. Rev. Lett.* **80**, 2338 (1998).
  - [28] S. C. Glotzer, *J. Non-Cryst. Solids* **274**, 342 (2000).
  - [29] H. Shiba, T. Kawasaki, and A. Onuki, *Phys. Rev. E* **86**, 041504 (2012).
  - [30] J. G. Gay and B. J. Berne, *J. Chem. Phys.* **74**, 3316 (1981).
  - [31] A. Ben-Naim, *J. Chem. Phys.* **54**, 3682 (1971); K. A. T. Silverstein, A. D. J. Haymet, and K. A. Dill, *J. Am. Chem. Soc.* **120**, 3166 (1998).
  - [32] J. M. Drouffe, A. C. Maggs and S. Leibler, *Science* **254**, 1353 (1991); H. Noguchi, *J. Chem. Phys.* **134**, 055101 (2011).
  - [33] S. Nosé, *Mol. Phys.* **52**, 255 (1984).
  - [34] D. R. Nelson and B. I. Halperin, *Phys. Rev. B* **19**, 2457 (1979).
  - [35] H. G. E. Hentschel, V. Ilyin, N. Makedonska, I. Procaccia, and N. Schupper, *Phys. Rev. E* **75**, 050404(R) (2007).
  - [36] T. Kawasaki and A. Onuki, *Phys. Rev. E* **87**, 012312 (2013). This paper shows that  $D\tau_b$  is nearly independent of  $T$  in a supercooled fragile binary mixture in three dimensions, where  $\tau_b$  is the bond breakage time [26].
  - [37] S. Sarkar, X. Ren, and K. Otsuka, *Phys. Rev. Lett.* **95**, 205702 (2005); Y. Wang, X. Ren, and K. Otsuka, *Phys. Rev. Lett.* **97**, 225703 (2006).
  - [38] R. A. Cowley, S.N. Gvasaliya, S.G. Lushnikov, B. Roessli, and G.M. Rotaru, *Adv. Phys.* **60**, 229 (2011).